RSC Advances

ROYAL SOCIETY OF CHEMISTRY

www.rsc.org/advances

Journal Name

COMMUNICATION

Enhanced amplified spontaneous emission from morphology-controlled organic-inorganic halide perovskite films

Received 00th January 20xx,
Accepted 00th January 20xx

DOI: 10.1039/x0xx00000x

www.rsc.org/

Liang Qin,[a] Longfeng Lv,[a] Yu Ning,[a] Chunhai Li,[a] Qipeng Lu,[a] Lijie Zhu,[a] Yufeng Hu,[a] Zhidong Lou,[a] Feng Teng[a] and Yanbing Hou*[a]

Organic-inorganic tri-halide perovskites ($MAPbX_3$, where MA = CH_3NH_3, and X = Cl, Br, I) have shown promise as laser gain media. The laser characteristics of perovskite films are susceptible to their crystallinity and morphology. Herein, we demonstrate morphology and crystalline of perovskite films could be well-controlled in a modified sequential deposition process by using binary solvent mixtures involving N,N-dimethylmethanamide (DMF) and dimethylsulfoxide (DMSO). The highly crystalline and notably smooth $MAPbI_3$ films on glass substrates yield outstanding amplified spontaneous emission (ASE) performance. The binary solvent engineering approach opens up new opportunities for the development of low-cost and high-efficient ASE devices based on perovskite materials.

Organic-inorganic tri-halide perovskites ($MAPbX_3$, where MA = CH_3NH_3, and X = Cl, Br, I) have attracted considerable attention due to their excellent photoelectric properties, such as high absorption coefficients, balanced long-range electron/hole transport lengths, low recombination rate, and tunable bandgap.[1-6] Tremendous efforts have been made to investigate halide perovskite-based materials for optoelectronic applications. Remarkably, the utilization of the optimized deposition process and device structure has achieved high-performance $MAPbX_3$ perovskite-based solar cells with the power conversion efficiencies exceeding 20%.[7] Recently, high brightness perovskite-based light-emitting diodes have been reported as well.[8] Notably, the $MAPbX_3$ perovskite materials have been confirmed greater than 70% photoluminescence (PL) quantum efficiency and lower than ~7 $\mu J/cm^2$ lasing threshold on a flexible cholesteric liquid crystal reflector,[9, 10] indicating its potential applications in laser devices as gain media for amplified spontaneous emission (ASE).

In most waveguide-based ASE devices, the scattering loss arises from irregularities in the waveguide walls and disorders in the crystal structure.[11, 12] It is well-known that the characteristics of morphology and crystalline of perovskite films are important factors in pursuing high-performance ASE devices.[13, 14] Therefore, both decreasing surface roughness and promoting crystallization of perovskite layer are beneficial to suppress the scattering loss efficiently.

However, the conventional solution-processed perovskite films possess the low crystallinity and rough surface, which results in high optical losses in waveguide-based lasing devices. Particularly, previous works have revealed that inhomogeneous perovskite films from two-step sequential deposition undergo a strong random scattering, consequently increasing light propagation loss.[6, 13, 15, 16] According to the literatures, solvent engineering in deposition processes has been demonstrated to be an effective strategy in controlling the morphology and crystallinity of the perovskite film, thus improves photoelectric performance.[15, 17-22] For example, the solution synthesis methods can optimize the size of the crystalline $MAPbI_3$ cuboids to promote the light harvesting and charge carrier extraction in solar cells.[13] Evaporation-induced self-assembly is also a novel method for the formation of highly crystalline perovskite materials.[16] Increasing the converting time could also promote the crystallization, but frustrating the surface morphology.[13] Meanwhile, the morphology of perovskite layers employing binary solvent engineering approaches are quite different, when films are deposited on different substrates, for instance, TiO_2/FTO, PEDOT:PSS/ITO and ZnO/ITO.[15, 23, 24] Obviously, the crystal growth together with film formation of perovskite materials is sensitive to the solvent composition and the substrates. However, there are very few reports about controlling morphology characteristics of perovskite materials deposited on glass substrates to obtain high-performance ASE devices. It is well-known that most of the ASE devices employ glass substrates, and the performance is susceptible to morphology and crystalline of films.[14, 25] Thus, it is essential to investigate the preparation of a smooth, dense, and continuous perovskite

[a] *Key Laboratory of Luminescence and Optical Information, Ministry of Education, Beijing JiaoTong University, Beijing 100044, China. E-mail: ybhou@bjtu.edu.cn*
Electronic Supplementary Information (ESI) available: XRD patterns, particle size, cross-section SEM images, AFM images, absorption spectra and PLQE. See DOI: 10.1039/x0xx00000x

film for achieving high-efficient perovskite ASE devices on glass substrates.

In this paper, we demonstrated that the morphology and the crystallinity of perovskite films could be well controlled by tuning the ratio of DMF and DMSO as a binary solvent mixture to dissolve the PbI_2 in a two-step sequential deposition process. The proper ratio of solvents yielded a smooth surface as well as highly crystalline, both of which improved the ASE performance. The gain and loss of the optimized waveguide were 91.84 cm^{-1} and 0.23 cm^{-1}, respectively. Meanwhile, the ASE threshold and the full width of half maximum (FWHM) were reduced to 54.10 $\mu J/cm^2$ and 8.16 nm, respectively. These results provide an important step forward by enhancing the performance of perovskite-based ASE device by means of the binary solvent engineering approach.

Fig. 1(a–f) show the SEM images of PbI_2 films which were spin coated from PbI_2 solutions that dissolved in DMF and DMSO mixtures in ratios of 10:0, 8:2, 6:4, 4:6, 2:8, and 0:10, respectively. Apparently, the morphology of the PbI_2 film from pure DMF solution (Fig. 1(a)) is markedly distinct from the case of DMSO (Fig. 1(f)). The PbI_2 film from DMF solution consist of large-size and anomalous crystals with a great quantity of pinholes, whereas that from DMSO solution has large amounts of needle-shaped PbI_2 crystals with slight pinholes. Moreover, as the PbI_2 DMF solution incorporated with a small number of DMSO solvent, there is inhibited-crystallization with smooth surface in the films as exhibited in Fig. 1(b-c). However, excessive amounts of DMSO bring about severely needle-shaped PbI_2 crystals as well as pinholes, as presented in Fig. 1(d-e).

Fig. 1. SEM images of PbI_2 films prepared from DMF-DMSO mixtures in 10:0 (a), 8:2 (b), 6:4 (c), 4:6 (d), 2:8 (e), and 0:10 (f) ratios (v/v).

Such changes of morphologies should be ascribed to the fact that solution-processed PbI_2 film is sensitive to the solvent environment.[26] On account of DMSO coordinating to PbI_2 more strongly in comparison to DMF, there is plenty of $PbI_2(DMSO)_2$ intermediate phase that can restrain crystallization strikingly in the case of using DMSO.[27] And the poor crystallinity was evidenced by the XRD patterns of PbI_2 films, as displayed in Fig. S1. Moreover, in consideration of its high boiling point (189 ^oC) and lower saturated vapor pressure (0.76 kPa at 60 ^oC), DMSO possesses the lower volatility compared to DMF with the lower boiling point (152.8 ^oC) and the higher saturated vapor pressure (3.46 kPa at 60 ^oC).[28] The vapor pressure of the DMF and DMSO mixture can be varied by tuning the solvent ratio as a result of strong interactions of hydrogen-bonding associations that exist between the mixture molecules.[29] The change of vapor pressure gives rise to the preferable morphology with smooth surface together with limited pinholes. Therefore, the addition of DMSO yields $PbI_2(DMSO)_2$ complexes inducing poor PbI_2 crystallization, and meanwhile assists in developing the smooth PbI_2 films. That kind of PbI_2 film should be beneficial to developing $MAPbI_3$ film with better morphology.

Fig. 2. SEM images of perovskite films converted from the PbI_2 films spin coated from the binary solvent solutions in 10:0 (a), 8:2 (b), 6:4 (c), 4:6 (d), 2:8 (e), and 0:10 (f) ratios.

Furthermore, the surface morphology of $MAPbI_3$ films was investigated by SEM measurements, as presented in Fig. 2 and Fig. S2. From the cross-sectional SEM (Fig. S2), the thickness of each perovskite film is consistent with the corresponding case measured by the surface profilometer, as summarized in table 1. The histogram of the average particle size of each $MAPbI_3$ film is shown in Fig. S3. It is obvious that $MAPbI_3$ films originating from binary solvent or pure DMSO solvent possess much smaller perovskite particles than pure DMF one. More importantly, the use of binary solvent engineering approach could obtain better morphology with much smoother surface compared to the case of single solvent. Considering that $MAPbI_3$ is converted from PbI_2, the transforming process should be associated with the PbI_2 film characteristics. When utilizing pure DMF solvent for PbI_2, the converting process is extremely fast. It is hard to control crystal growth, thus forming $MAPbI_3$ films with the rough surface as well as large and heterogeneous particles, as shown in Fig. 2(a) and Fig. S2(a). By using DMF and DMSO mixture solvent, the presence of $PbI_2(DMSO)_2$ complexes can help control the growth of perovskite crystal in the subsequent deposition process, which yields the smooth surface with small and homogeneous particles. Clearly, DMSO serving as an additive can control the reaction dynamics and equilibrate reaction probability of PbI_2 complexes with MAI solutions.[30] However, for the case using pure DMSO solvent, $MAPbI_3$ particles assemble into mulberry-shaped clusters attached on the surface, markedly increasing the film roughness.

In order to fully estimate surface roughness of these perovskite films, surface atomic force microscope (AFM) measurements were performed. As presented in Fig. S4, the surfaces of the $MAPbI_3$ films with DMSO additives are much smoother than that of the film with pure DMF solvent that the root mean square (RMS) roughness (Rq) is 38.61 nm. With different ratio addition of DMSO (DMF and DMSO mixtures in ratios of 8:2, 6:4, 4:6, 2:8, and 0:10), the Rq are 10.38, 8.49, 11.05, 11.72 and 15.19 nm respectively. By optimizing the binary solvent ratio, the best-quality $MAPbI_3$ films are achieved at a DMF: DMSO ratio of 6:4 (v/v). In particular, the optimized films are pinhole-free and uniform, which may be suitable for the high-performance ASE devices. Such $MAPbI_3$ films should address this issue that perovskite films prepared from the conventional process are not suitable for the need of high-performance ASE devices.

Fig. 3. XRD patterns (a) and UV-vis absorption spectra (b) of the perovskite films.

To gain insight into the binary solvent engineering effect on crystallization and light absorption of the $MAPbI_3$ thin films, the XRD and UV-vis absorption spectra were performed, as shown in Fig. 3. Crystalline structural analysis by using XRD

(Fig. 3(a)) suggests that the extent of reaction from PbI_2 based on varied solvents to $MAPbI_3$ films is different. The more DMSO used, the more complete conversion could be achieved, which is also verified by the corresponding absorption spectra (Fig. 3(b)). The DMF-based $MAPbI_3$ film possesses a much stronger absorption at around 500 nm than the case using pure DMSO solvent. The absorption shoulder of approximately 500 nm comes from the characteristic band-gap absorption of crystalline PbI_2 (Fig. S5).[30] The use of DMSO solvent for PbI_2 improves the conversion of the PbI_2 $(DMSO)_2$ complexes into $MAPbI_3$ films. The above results also demonstrate that the conversion rate from PbI_2 to $MAPbI_3$ can be well controlled by changing the ratio of DMSO in the binary solvent mixture.

Fig. 4. Schematic of the optical measurement setup (a) and the output spectra of the $MAPbI_3$ film under the excitation at different pump intensities (b).

The ASE performances of the samples were measured with the setup shown in Fig. 4(a). All samples were optically pumped at 500 nm by an optical parametric oscillator that delivered 5-ns pulses at a repetition rate of 10 Hz, itself pumped by a Q-switched, neodymium ion-doped, yttrium aluminum garnet (Nd^{3+}:YAG) laser. The intensity of the laser was adjusted with neutral density filters of different transmittance. A 0.5 × 3 mm^2 laser excitation strip was focused on the $MAPbI_3$ film with a cylindrical lens and an adjustable slit. The emitting light from the edge of $MAPbI_3$ films was collected by a multimode fiber in a direction perpendicular to the pump laser beam through a cut-off filter and measured with a CCD spectrograph. All measurements were carried out under ambient conditions. Fig. 4(b) presents the normalized emission spectra of the 6:4 perovskite films under various pump intensities. With increasing pump intensity, the FWHM decreases significantly and shows an abrupt decrease above the threshold of 54.10 μJ/cm^2. The FWHM of the emission spectrum reaches a minimum value of about 8 nm at 114.55 μJ/cm^2.

To characterize the ASE performances of the different samples quantitatively, we calculated the ASE parameters for all the samples. The pump intensity effect on the output emission and the FWHM of each $MAPbI_3$ film under the excitation by a 500-nm laser are shown in Fig. 5(a-b), respectively. From both figures, it can be found that the ASE intensity and FWHM are improved by the addition of DMSO to the DMF solution. The sample prepared with a 6:4 solvent ratio exhibits the highest ASE output at the same excitation intensity. It is well-known that the waveguide structure is of great importance for high-performance ASE devices because the spontaneously emitted photons are guided along the surface and the strip-shaped gain region amplifies them by stimulated emission.[31] On the basis of the 6:4 perovskite sample morphology analysis, it possesses the smoother surface with much smaller particles than other cases, thus effectively suppressing light scatter at the surface and in the internal of films. Such preferable film constructs a nearly perfect planar waveguide, which boosts the ASE performance.

Table 1. ASE characteristics of each PbI_2 (solvent)-based perovskite film.[a]

DMF:DMSO (v/v)	Thickness (nm)	RMS Roughness (nm)	Threshold (μJ/cm^{-2})	Gain (cm^{-1})	Loss (cm^{-1})	FWHM (nm)	PLQE (%)
10 : 0	350 ± 22	38.61 ± 4.17	114.55 ± 0.12	27.72 ± 0.04	6.66 ± 0.08	10.44 ± 0.05	6.75 ± 0.21
8 : 2	330 ± 16	10.38 ± 1.05	55.02 ± 0.08	78.34 ± 0.19	1.48 ± 0.03	8.46 ± 0.02	16.98 ± 0.07
6 : 4	320 ± 12	8.49 ± 0.99	54.10 ± 0.04	91.84 ± 0.23	0.23 ± 0.05	8.16 ± 0.02	18.42 ± 0.13
4 : 6	330 ± 23	11.05 ± 1.61	93.18 ± 0.05	51.04 ± 0.11	2.48 ± 0.03	8.61 ± 0.03	13.75 ± 0.06
2 : 8	330 ± 15	11.72 ± 1.07	103.82 ± 0.11	46.13 ± 0.05	3.21 ± 0.03	8.86 ± 0.06	10.97 ± 0.19
0 : 10	340 ± 14	15.19 ± 2.35	108.14 ± 0.09	42.83 ± 0.07	3.38 ± 0.01	9.44 ± 0.08	10.69 ± 0.05

[a] All the parameters are the average of a batch of 5 devices.

Fig. 5. The pump intensity effect on the output intensity (a) and FWHM (b), the dependence of output intensity on excitation length (c), and un-pumped region (d) of the perovskite films prepared from solvent blends at different ratios.

In order to profoundly understand the ASE characteristics of a waveguide based on perovskite film, the gain and loss of each sample were studied in detail. The net gain was calculated by the usual variable-strip-length method in which the relationship between ASE emission $I(\lambda)$ and the length of excitation strip can be given by the following equation.[25, 32, 33]

$$I(\lambda) = \frac{A(\lambda)I_p}{g(\lambda)}\left(e^{g(\lambda)L} - 1\right) \quad (1)$$

where $A(\lambda)$ is a constant related to the cross section for spontaneous emission, I_p is the pump intensity, $g(\lambda)$ is the net gain coefficient, and L is the length of the pumped strip. Fig. 5(c) shows the excitation length dependences of ASE intensity of 6 samples at a pump intensity of 114.55 μJ/cm^2. The solid curve in Fig. 5(c) is a linear fit of the initial part of the half-logarithmic plot of the experimental data. The gain for each sample was fitted for the liner part and summarized in Table 1. From this table, it is clear that adding DMSO facilitates increasing the gain. Normally, the gain increase of ASE device can be attributed to the enhanced PL efficiency,[14, 34-36] which is also seen in these results in the PL efficiency measurements shown in Fig. S6 and summarized in Table 1.

The loss coefficient of the waveguide was measured using a regular method in which the pumped length was kept constant (L = 3 mm) and the pumped region was moved away from the edge of the waveguide. Because the excitation of the pump strip remains constant, the detected ASE output from the edge of the sample decreases as the un-pumped region

from the end of the pump region to the edge increases in length with the following equation.[32, 37]

$$I = I_0 e^{-\alpha x} \quad (2)$$

where α is the waveguide loss coefficient and x is the length of the un-pumped region from the end of the pump region to the edge of the sample. The dependence of the ASE output on the length of un-pumped region of all samples are shown in Fig. 5(d). Based on these results, the loss coefficients of different samples can be fitted by equation (2). Comparing the loss coefficients of different samples (Table 1), the introduction of DMSO significantly reduces loss in the $MAPbI_3$ waveguide. The loss in the 6:4 sample is only several percent of the pure DMF sample. The smoother surface increases total reflection and decreases the light propagation loss.

All the ASE parameters of the perovskite films are summarized in Table 1. Referring to the XRD and SEM results, decreasing the ratio of DMF:DMSO from 10:0 to 6:4, significantly improves the ASE parameters because of the reduction in the size of $MAPbI_3$ crystalline particles and the formation of the ultra-smooth surface, which decreases loss in the $MAPbI_3$ films significantly. When continuing to decrease the ratio from 6:4 to 0:10, their performance become poor, which should be attributed to the increase in the particle size and the formation of the mulberry-shaped clusters.

Conclusions

In summary, we have demonstrated a mixture of DMF and DMSO as the solvent for PbI_2 to develop smooth, dense, and highly crystalline $MAPbI_3$ perovskite thin films via sequential deposition on glass substrates. The crystallinity and morphology of the $MAPbI_3$ perovskite films could be well controlled by changing the solvent ratio of DMF and DMSO. The optimized sample (volume ratio, DMF:DMSO = 6:4) exhibits excellent ASE performance, which proves that the binary solvent engineering is an effective strategy for the fabrication of uniform PbI_2 (solvent)-based perovskite layers with well-controlled crystallinity and morphology. Our results clearly indicate binary solvent engineering approach can provide an excellent pathway for achieving high-performance and cost-effective perovskite-based ASE as well as laser devices.

Experimental section

Sample preparation

Perovskite films were prepared via a modified sequential deposition process in which the PbI_2 films were spin coated from the precursor solution containing 1 mol/L of PbI_2 (99%, Alfa Aesar) in a binary solvent mixture of DMF (99.8%, Alfa Aesar) and DMSO (99.8%, Alfa Aesar) in different volume ratios (10:0, 8:2, 6:4, 4:6, 2:8, 0:10, v/v). Sequentially, the obtained PbI_2 (solvent) complex thin films were dried at 50 °C for 20 min. Then, PbI_2 films were dipped into an isopropanol (99.7%, Alfa Aesar) solution of methylammonium iodide (MAI, 99%, Dyesol) at 40 °C for 2 min to convert the PbI_2 complex to $MAPbI_3$. Finally, the $MAPbI_3$ thin films were dried at 70°C for 40 min. The whole process of thin film preparation was performed in a nitrogen filled glove box.

Film characterization

A field emission scanning electron microscope (FE-SEM, Hitachi-S4800) was used to obtain SEM images. The X-ray diffraction (XRD) patterns were recorded using a Bruker D8 Advance X-ray diffractometer. The thicknesses of the films were measured by Ambios Technology XP-2 surface profilometer. Ultraviolet-visible (UV-vis) absorption spectra were collected on the Shimadzu UV-3101PC spectrometer. A Continuum SureLite II Nd^{3+}: YAG laser pumping a Continuum SureLite optical parametric oscillator (OPO) was employed as the excitation source for ASE measurements of perovskite films. The laser pulse energy was detected with a Coherent J-10SI-HE power meter. The emission spectra were performed using an Acton-150 imaging spectrophotometer.

Acknowledgements

This research is supported by the Natural Science Foundation of China (Grant Nos. 61275175, 61177017, 61377028, 61036007), the National Science Foundation for Distinguished Young Scholars of China (61125505), and the Fundamental Research Funds for the Central University (2014JBZ009).

Notes and references

1 G. Xing, N. Mathews, S. Sun, S. S. Lim, Y. M. Lam, M. Gratzel, S. Mhaisalkar and T. C. Sum, *Science*, 2013, **342**, 344-347.
2 M. A. Green, A. Ho-Baillie and H. J. Snaith, *Nat. Photonics*, 2014, **8**, 506-514.
3 H. S. Kim, C. R. Lee, J. H. Im, K. B. Lee, T. Moehl, A. Marchioro, S. J. Moon, R. Humphry-Baker, J. H. Yum, J. E. Moser, M. Gratzel and N. G. Park, *Sci. Rep.*, 2012, **2**, 591.
4 J. H. Heo, S. H. Im, J. H. Noh, T. N. Mandal, C. S. Lim, J. A. Chang, Y. H. Lee, H. J. Kim, A. Sarkar, M. K. Nazeeruddin, M. Gratzel and S. I. Seok, *Nat. Photonics*, 2013, **7**, 487-492.
5 H. Zhou, Q. Chen, G. Li, S. Luo, T. B. Song, H. S. Duan, Z. Hong, J. You, Y. Liu and Y. Yang, *Science*, 2014, **345**, 542-546.
6 G. Xing, N. Mathews, S. S. Lim, N. Yantara, X. Liu, D. Sabba, M. Gratzel, S. Mhaisalkar and T. C. Sum, *Nat. Mater.*, 2014, **13**, 476-480.
7 W. S. Yang, J. H. Noh, N. J. Jeon, Y. C. Kim, S. Ryu, J. Seo and S. I. Seok, *Science*, 2015, **348**, 1234-1237.
8 Z. K. Tan, R. S. Moghaddam, M. L. Lai, P. Docampo, R. Higler, F. Deschler, M. Price, A. Sadhanala, L. M. Pazos, D. Credgington, F. Hanusch, T. Bein, H. J. Snaith and R. H. Friend, *Nat. Nanotechnol.*, 2014, **9**, 687-692.
9 F. Deschler, M. Price, S. Pathak, L. E. Klintberg, D. D. Jarausch, R. Higler, S. Huttner, T. Leijtens, S. D. Stranks, H. J. Snaith, M. Atature, R. T. Phillips and R. H. Friend, *J. Phys. Chem. Lett.*, 2014, **5**, 1421-1426.
10 S. D. Stranks, S. M. Wood, K. Wojciechowski, F. Deschler, M. Saliba, H. Khandelwal, J. B. Patel, S. J. Elston, L. M. Herz, M. B. Johnston, A. P. H. J. Schenning, M. G. Debije, M. K. Riede, S. M. Morris and H. J. Snaith, *Nano Lett.*, 2015, **15**, 4935-4941.

11 F. Payne and J. Lacey, *Opt. Quant. Electron.*, 1994, **26**, 977-986.
12 R. Kabe, H. Nakanotani, T. Sakanoue, M. Yahiro and C. Adachi, *Adv. Mater.*, 2009, **21**, 4034-4038.
13 J. H. Im, I. H. Jang, N. Pellet, M. Gratzel and N. G. Park, *Nat. Nanotechnol.*, 2014, **9**, 927-932.
14 V. D'Innocenzo, A. R. Srimath Kandada, M. De Bastiani, M. Gandini and A. Petrozza, *J. Am. Chem. Soc.*, 2014, **136**, 17730-17733.
15 N. J. Jeon, J. H. Noh, Y. C. Kim, W. S. Yang, S. Ryu and S. I. Seok, *Nat. Mater.*, 2014, **13**, 897-903.
16 Z. Xiao, Q. Dong, C. Bi, Y. Shao, Y. Yuan and J. Huang, *Adv. Mater.*, 2014, **26**, 6503-6509.
17 S. Paek, N. Cho, H. Choi, H. Jeong, J. S. Lim, J.-Y. Hwang, J. K. Lee and J. Ko, *J. Phys. Chem. C*, 2014, **118**, 25899-25905.
18 Q. Chen, H. Zhou, T.-B. Song, S. Luo, Z. Hong, H.-S. Duan, L. Dou, Y. Liu and Y. Yang, *Nano Lett.*, 2014, **14**, 4158-4163.
19 F. X. Xie, D. Zhang, H. Su, X. Ren, K. S. Wong, M. Grätzel and W. C. H. Choy, *ACS nano*, 2015, **9**, 639-646.
20 R. Kang, J.-E. Kim, J.-S. Yeo, S. Lee, Y.-J. Jeon and D.-Y. Kim, *J. Phys. Chem. C*, 2014, **118**, 26513-26520.
21 S. T. Ha, X. Liu, Q. Zhang, D. Giovanni, T. C. Sum and Q. Xiong, *Adv. Optical Mater.*, 2014, **2**, 838-844.
22 Q. Zhang, S. T. Ha, X. Liu, T. C. Sum and Q. Xiong, *Nano Lett.*, 2014, **14**, 5995-6001.
23 Y. Rong, Z. Tang, Y. Zhao, X. Zhong, S. Venkatesan, H. Graham, M. Patton, Y. Jing, A. M. Guloy and Y. Yao, *Nanoscale*, 2015, **7**, 10595-10599.
24 S. Ito, S. Tanaka and H. Nishino, *J. Phys. Chem. Lett.*, 2015, **6**, 881-886.
25 M. D. McGehee and A. J. Heeger, *Adv. Mater.*, 2000, **12**, 1655-1668.
26 G. E. Eperon, V. M. Burlakov, P. Docampo, A. Goriely and H. J. Snaith, *Adv. Funct. Mater.*, 2014, **24**, 151-157.
27 H. Miyamae, Y. Numahata and M. Nagata, *Chem. Lett.*, 1980, **9**, 663-664.
28 M. NISHIMURA, M. NAKAYAMA and T. YANO, *J. Chem. Eng. Jpn.*, 1972, **5**, 223-226.
29 X. Qian, B. Han, Y. Liu, H. Yan and R. Liu, *J. Solution Chem.*, 1995, **24**, 1183-1189.
30 Y. Wu, A. Islam, X. Yang, C. Qin, J. Liu, K. Zhang, W. Peng and L. Han, *Energ. Environ. Sci.*, 2014, **7**, 2934-2938.
31 B. Zhang, Y. Hou, F. Teng, Z. Lou, X. Liu and Y. Wang, *Appl. Phys. Lett.*, 2010, **96**, 103303.
32 M. D. McGehee, R. Gupta, S. Veenstra, E. K. Miller, M. A. Diaz-Garcia and A. J. Heeger, *Phys. Rev. B*, 1998, **58**, 7035.
33 K. Shaklee and R. Leheny, *Appl. Phys. Lett.*, 1971, **18**, 475-477.
34 R. Xia, P. N. Stavrinou, D. D. C. Bradley and Y. Kim, *J. Appl. Phys.*, 2012, **111**, 123107.
35 B. K. Yap, R. Xia, M. Campoy-Quiles, P. N. Stavrinou and D. D. C. Bradley, *Nat. Mater.*, 2008, **7**, 376-380.
36 R. Xia, G. Heliotis, Y. Hou and D. D. C. Bradley, *Org. Electron.*, 2003, **4**, 165-177.
37 Y. Sorek, R. Reisfeld, I. Finkelstein and S. Ruschin, *Appl. Phys. Lett.*, 1995, **66**, 1169-1171.

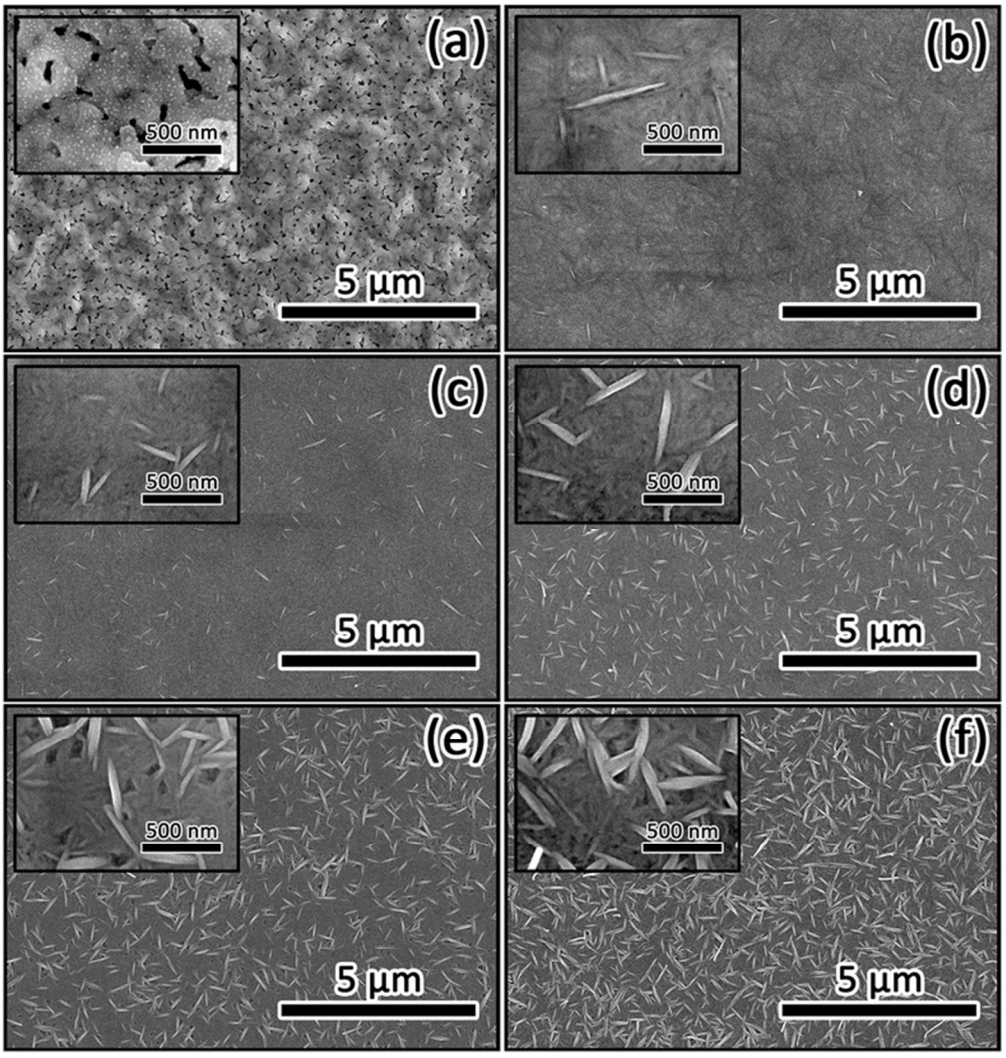

66x69mm (300 x 300 DPI)

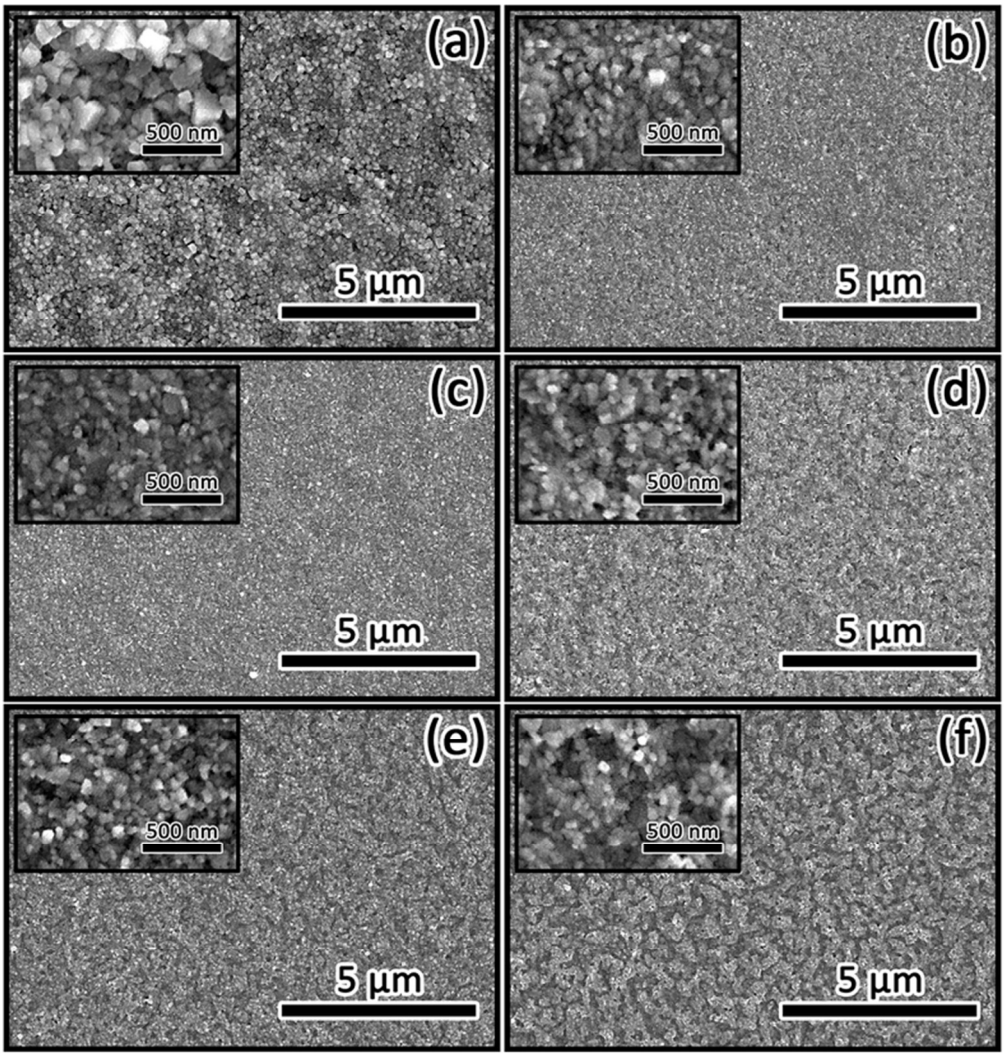

66x69mm (300 x 300 DPI)

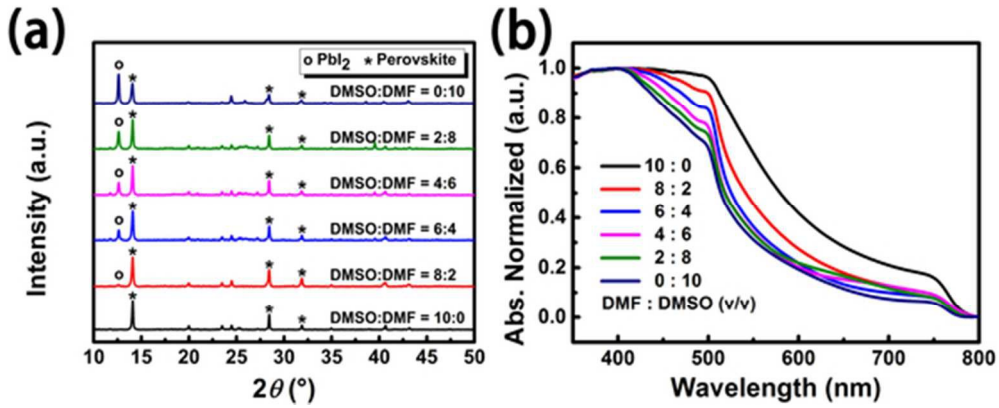

50x20mm (300 x 300 DPI)

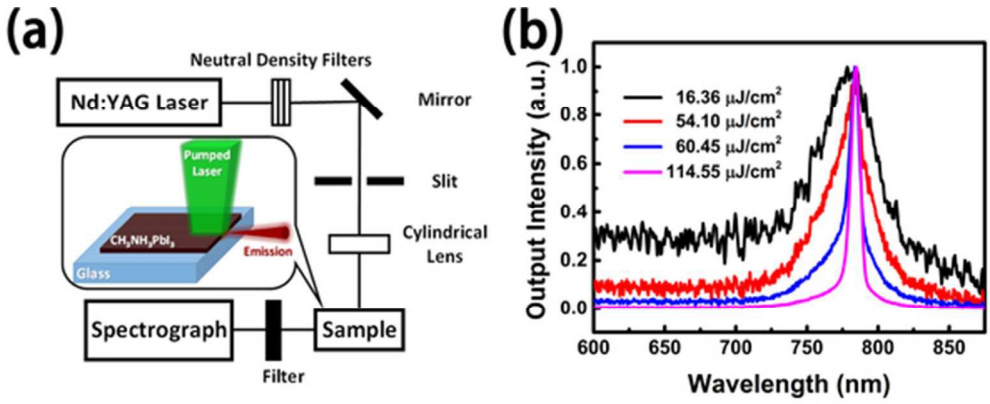

50x20mm (300 x 300 DPI)

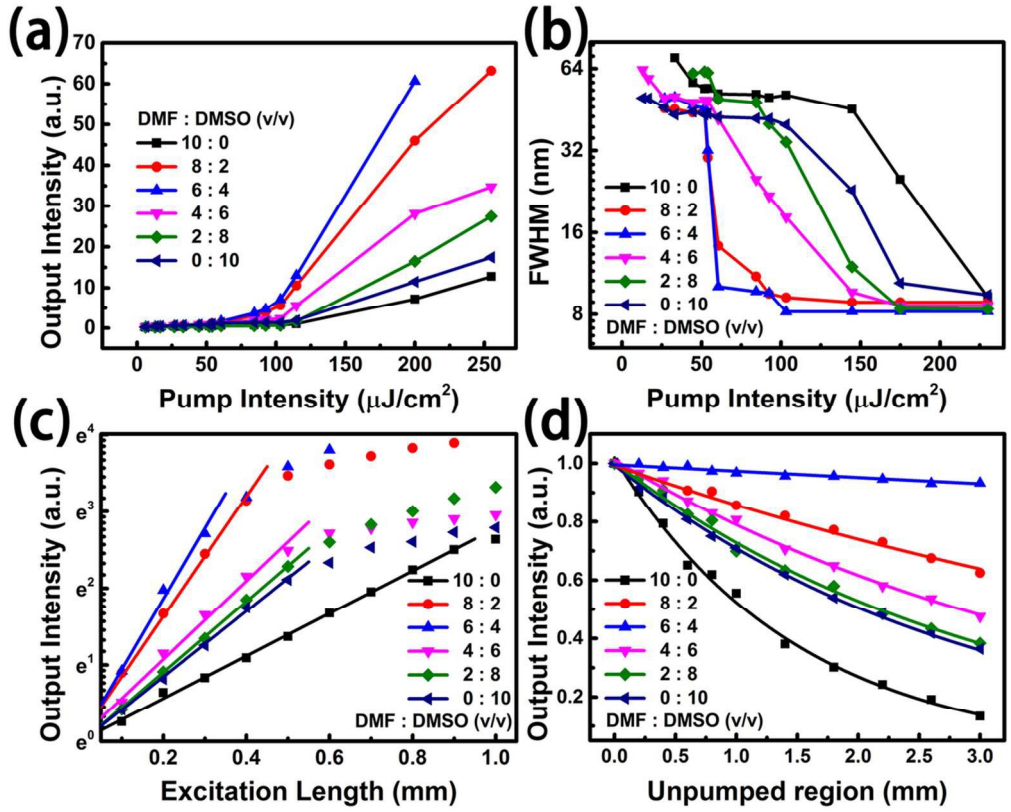

102x82mm (300 x 300 DPI)

Perovskite films with well-controlled crystallinity and morphology in a modified sequential deposition process by using binary solvent mixtures involving N,N-dimethylmethanamide and dimethylsulfoxide that exhibit excellent amplified spontaneous emission performances with threshold of 54.10 μJ/cm^2 and full width of half maximum of 8.16 nm at 780 nm.